Peer review status:

This is a non-peer-reviewed preprint submitted to EarthArXiv.

Title：Retrieval of Cloud Optical Thickness Based on FY-4B Geostationary Satellite Multichannel Data Combined with Machine Learning

Author：Xiangqian Wei[1,*],

1. Hanjiang Normal University

*. Correspondence: weixiangqian@hjnu.edu.cn

Retrieval of Cloud Optical Thickness Based on FY-4B Geostationary Satellite Multichannel Data Combined with Machine Learning

Xiangqian Wei[1,*],

1. Hanjiang Normal University

*. Correspondence: weixiangqian@hjnu.edu.cn

Abstract: Accurate real-time retrieval of cloud optical thickness (COT) is of great significance for meteorological operations and climate research. To address the limitations of traditional physical methods, which rely on prior parameters, exhibit slow response times, and suffer from poor adaptability, this study proposes a COT retrieval method based on multichannel data from the FY-4B geostationary satellite combined with machine learning. Using FY-4B visible (0.65 μm) and near-infrared (3.7 μm) data as inputs and high-precision COT products from the FY-3F polar-orbiting satellite as ground truth, a total of 342 valid samples were constructed through spatiotemporal matching and quality control. Two neural network models were designed to achieve end-to-end retrieval. The results indicate that Model A, which employs a decoupled feature extraction strategy, achieves the best performance, with a correlation coefficient of 0.770 and a root mean square error of 4.532 relative to the measured values, along with good spatiotemporal consistency. This approach overcomes the observational limitations of polar-orbiting satellites and provides a new pathway for intelligent cloud parameter retrieval.

Keywords: cloud optical thickness; FY-4B; geostationary satellite; machine learning; neural network; remote sensing retrieval

1.Introduction

Clouds play a central role in regulating the energy balance and hydrological cycle of the Earth–atmosphere system. Cloud optical thickness (COT), a key parameter characterizing the attenuation of solar radiation by clouds, directly reflects cloud layer thickness, condensate content, and vertical structure, and maintains a well-defined physical relationship with cloud geometric thickness and effective droplet radius[1][2][3]. In operational applications, accurate and real-time COT retrievals are essential for nowcasting precipitation, identifying severe convective cloud clusters, and enabling quantitative precipitation estimation. They also provide critical support for weather modification operations, aircraft icing risk warnings, and solar energy resource

assessment[4][5][6]. In research contexts, COT serves as a fundamental input for calculating atmospheric radiative budgets, constraining climate models, and investigating aerosol–cloud interactions, with the accuracy and timeliness of retrievals directly determining the reliability of such studies[7][8][9][10][11].

Current mainstream COT retrieval methods are primarily based on traditional physical models, including lookup table approaches using radiative transfer models such as SBDART and 6S, optimal estimation methods, and empirical statistical regression techniques[12][13]. While these methods are physically transparent and form the algorithmic basis for existing satellite COT products, they face significant challenges in large-scale operational applications. First, they rely heavily on a priori inputs such as surface albedo and atmospheric profiles, requiring multi-source observational data from weather radars and radiosondes, which incur high acquisition costs, complex processing workflows, and long processing times[14]. Second, the computational complexity of radiative transfer simulations and lookup table matching leads to long operational latency, making it difficult to meet the real-time demands of nowcasting[15]. Third, their adaptability across diverse cloud scenes remains limited; they struggle with both the weak signals from thin cirrus clouds and the saturation issues in thick convective clouds, resulting in substantially reduced accuracy under heterogeneous cloud conditions[16][17][18][19].

The emergence of machine learning methods has provided a new pathway for the operational retrieval of cloud optical thickness (COT). Characterized by an end-to-end retrieval paradigm, these approaches eliminate the need for complex radiative transfer simulations and manual a priori inputs, enabling the automatic extraction of deep-level features such as spatial texture and inter-band correlations from multispectral satellite data[20][21][22][23]. Furthermore, the inference speed of a trained model can be exceptionally fast, meeting the requirements of both real-time performance and adaptability to complex scenarios[24][25][26]. To this end, this paper proposes a COT retrieval method based on multispectral data from the FY-4B geostationary satellite combined with deep learning. Leveraging the advantages of FY-4B's high temporal resolution (minute-level) and multispectral (visible to infrared) observations, the method captures the dynamic evolution of cloud systems in real time. High-precision COT products from the FY-3F polar-orbiting satellite are used as ground truth labels to construct a spatiotemporally complementary training dataset, thereby overcoming the operational bottlenecks of traditional methods and addressing the reliance on simulated data that characterizes existing machine learning-based approaches.

The remainder of this paper is structured as follows. Chapter 2 provides a detailed description of the study data and the construction of the dataset. Chapter 3 presents the retrieval model architecture and training strategy. Chapter 4 describes the model validation and analysis of results. Chapter 5 discusses the limitations of the model and directions for future optimization. Chapter 6 concludes the paper.

2. Dataset Construction Methodology

2.1 Data Sources and Key Characteristics

This study utilizes data from China's Fengyun series of satellites, with the study area covering China and the surrounding Asia-Pacific region (70°E–140°E, 15°N–55°N). Model inputs are derived from the core channel data of the Advanced Geostationary Radiation Imager (AGRI) onboard the FY-4B geostationary satellite for the year 2025[27][28], including the visible (0.65 μm) and near-infrared (3.7 μm) channels. The data have a temporal resolution of 15 minutes and a spatial resolution of 4 km for the visible and infrared channels, with the original data stored in image format.

The cloud optical thickness (COT) product retrieved from the Medium Resolution Spectral Imager II (MERSI-LL) onboard the FY-3F polar-orbiting satellite during the same period is selected as the ground truth label. The satellite operates on a sun-synchronous orbit at an altitude of 830 km, with a single daily overpass (local time 10:30–11:30) and a spatial resolution of 5 km. The retrieval accuracy of the valid data is better than 15%. The product includes fields for COT, cloud phase, and quality flags, and is stored in HDF5 format.

2.2 Data Preprocessing and Spatiotemporal Matching

The FY-4B data undergo coordinate calibration and georeferencing, followed by bilinear interpolation to uniformly resample all channels onto a 0.1° × 0.1° equal-latitude-longitude grid. Abnormal pixels affected by radiance saturation or calibration failure are removed. The FY-3F products are subjected to geographic coordinate correction and then interpolated onto the same unified grid using the inverse distance weighting method, with simultaneous spatial matching of cloud phase and quality flags.

For temporal matching, the FY-3F overpass center time is used as the reference, and the nearest FY-4B observations within a ±15-minute window are paired. Spatially, a pixel-to-pixel correspondence between inputs and labels is achieved based on the unified grid.

2.3 Quality Control and Dataset Partitioning

A three-tier quality control procedure is implemented to screen valid samples:

① Physical outliers with COT < 0 or COT > 100, as well as pixels with invalid quality flags, are removed.

② Sample groups with a cloud region overlap ratio between the two satellites of at least 80% are retained.

③ Sample groups in which invalid pixels account for more than 20% of the total are excluded. Following this procedure, a total of 342 valid sample groups are obtained.

For dataset partitioning, a temporal stratified random partitioning strategy is adopted. Each month is divided into three subsets (early, middle, and late ten-day periods), and each subset is divided into training, validation, and test sets at a ratio of 7:1:2. During training, temporal reshuffling is applied to enhance sample diversity, with samples grouped in batches of four to form training combinations.

3. Neural Network Model Architecture

Traditional physical methods for retrieving cloud optical thickness rely on radiative transfer models, such as SBDART, to simulate the contributions of various radiative pathways. However, these methods require precise a priori parameters, including surface albedo and atmospheric profiles, and involve substantial computational complexity.

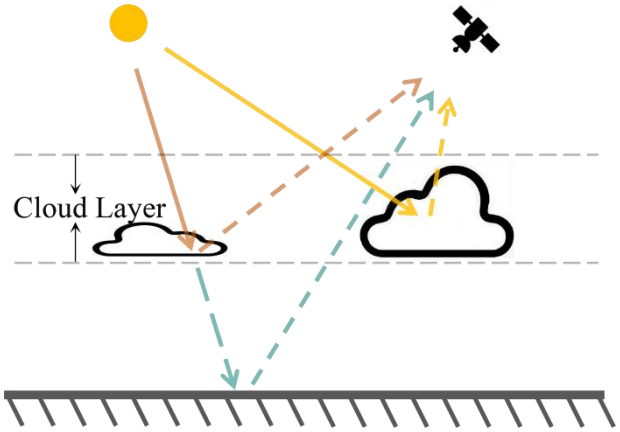

Figure 1 Schematic diagram of the radiative transfer path observed by the satellite.

As illustrated in Figure 1, the diagram depicts the reflection path of light by clouds. Optical thickness characterizes the degree of attenuation of direct solar radiation by the cloud layer. A portion of the solar radiation obstructed by the cloud is reflected toward the satellite receiver. Consequently, a distinct relationship exists between satellite remote sensing imagery and cloud optical thickness.

Neural network methods, through end-to-end learning, can automatically extract key features associated with in-cloud reflection, thereby avoiding reliance on complex physical models while simultaneously improving retrieval efficiency and adaptability to diverse scenarios.

3.1 Overall Model Computational Framework

In this study, two neural network models are designed to achieve end-to-end COT retrieval. Both models take FY-4B multispectral fusion data as input, adapt to the

observational characteristics of polar-orbiting satellites, and optimize the error only over effective observation regions.

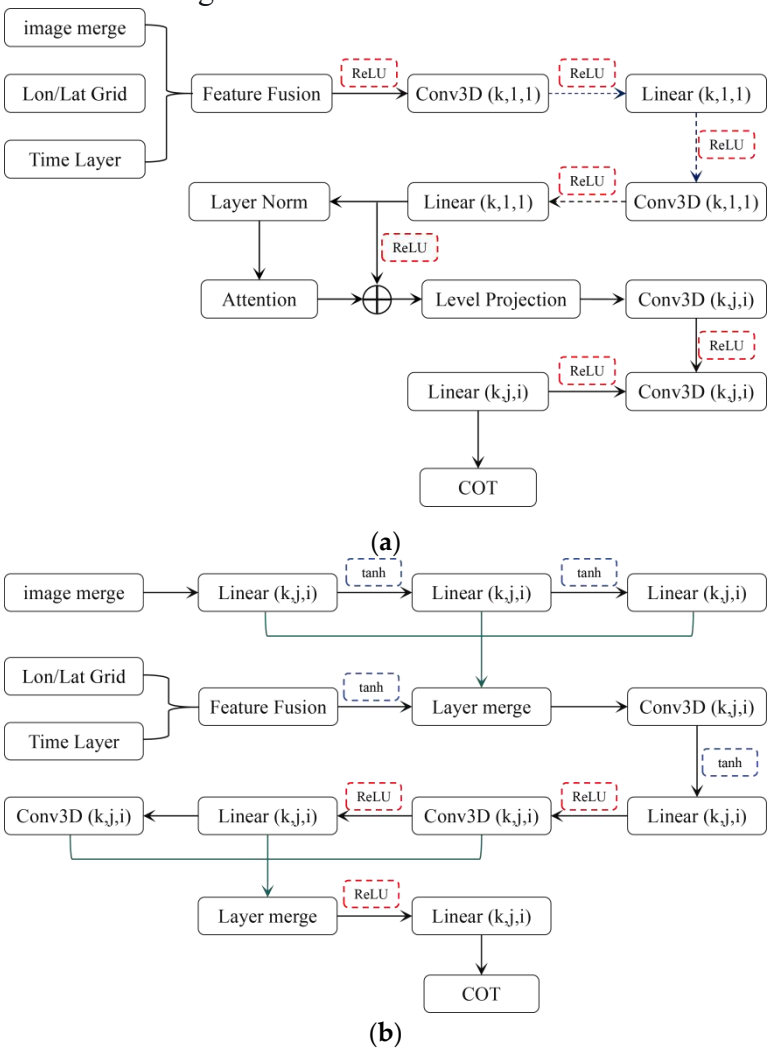

Figure 2 Flowchart framework of the two models. (a) Model A; (b) Model B.

As illustrated in Figure 2, Model A adopts a decoupled design that prioritizes the extraction of vertical dimensional features to reduce computational redundancy. Model B employs an end-to-end full extraction architecture that fully exploits three-dimensional spatiotemporal correlations. A comparative validation is conducted to evaluate the applicability of the vertical feature decoupling strategy.

3.2 Model A

As illustrated in Figure 2a, Model A adopts a design philosophy of "vertical dimension prioritization supplemented by global feature extraction." After inputting multispectral fused images, latitude–longitude grids, and temporal features, the model employs Conv3D (k,1,1) and Linear (k,1,1) layers to extract core features along the vertical dimension. The Level Projection layer subsequently performs vertical information fusion, followed by Layer Normalization and attention mechanism enhancement. Through Linear (k,j,i) and Conv3D (k,j,i) layers, three-dimensional

global feature fusion is accomplished, and the final COT result is output after ReLU activation. Specifically, the Level Projection layer first expands the number of vertical levels to a specified count of 2n layers and then reduces them to n layers via convolution, thereby achieving information fusion along the vertical direction.

3.3 Model B Computational Workflow

As illustrated in Figure 2b, Model B adopts a framework of "full three-dimensional extraction and iterative multilevel fusion." After integrating the multisource input features, Conv3D (k,j,i) and Linear (k,j,i) layers are used to simultaneously extract three-dimensional spatiotemporal features. Nonlinear expressiveness is enhanced through multiple rounds of ReLU activation. Layer merge operations are employed to superimpose and fuse features from different levels, and the "Conv3D/Linear + ReLU" modules are iteratively applied to deepen feature mining, ultimately producing the COT result directly.

3.2 Model Training Configuration

Framework and Data: Implemented using PyTorch 2.0, with the training data consisting of a spatiotemporally matched cloud optical thickness dataset derived from FY-4B and FY-3F.

Optimization Strategy: The AdamW optimizer is employed with a weight decay of 1e-4 and an initial learning rate of 0.001. This is combined with a cosine annealing scheduler (T_max=100, minimum learning rate=1e-6) and an early stopping mechanism that terminates training if the validation loss does not decrease for 30 consecutive epochs. Mixed precision training (FP16) is adopted.

Loss Function: A masked mean squared error (Masked MSE) is utilized to compute the loss exclusively over valid observation regions, thereby avoiding interference from non-observed areas. The formula is as follows:

$$MSE = \frac{1}{N_{valid}} \sum_{i=1}^{N} (y_i - y_{simu,i})^2 \qquad (1)$$

Here, N_{valid} denotes the number of valid samples, y_i represents the true Cloud Optical Thickness (COT) value of the i-th sample (derived from FY-3F data), and $y_{simu,i}$ is the corresponding simulated value from the model.

This loss function effectively avoids the interference of invalid errors from unobserved regions during training, focusing on optimizing model parameters with valid data. It has a smooth gradient and is computationally efficient, enabling stable model convergence.

3.3 Model Performance Evaluation

To comprehensively quantify the retrieval accuracy of the model, three core

metrics are employed on an independent test set, collectively assessing the error magnitude, dispersion, linear correlation, and explanatory power:

(1) Mean Absolute Error (MAE)

$$MAE = \frac{1}{N}\sum_{i=1}^{N}\left|y_i - y_{simu,i}\right| \quad (2)$$

(2) Root Mean Square Error (RMSE)

$$RMSE = \sqrt{\frac{1}{N}\sum_{i=1}^{N}(y_i - y_{simu,i})^2} \quad (3)$$

(3) Correlation Coefficient (CC)

$$CC = \frac{\sum_{i=1}^{N}(y_i-\bar{y})(y_{simu,i}-\overline{y_{simu}})}{\sqrt{\sum_{i=1}^{N}(y_i-\bar{y})^2\sum_{i=1}^{N}(y_{simu,i}-\overline{y_{simu}})^2}} \quad (4)$$

Here, N denotes the total number of samples, y_i represents the true Cloud Optical Thickness (COT) value of the i-th sample (derived from FY-3F data), $\bar{y}$ is the mean value of the sample y, $y_{simu,i}$ is the simulated value, and $\overline{y_{simu,i}}$ is the mean value of the simulated values.

These metrics comprehensively evaluate model performance from four dimensions: error magnitude, error distribution, linear correlation, and model explanatory power.

4.Result

This chapter evaluates the COT retrieval performance of two models (Model A and Model B) from the perspectives of quantitative accuracy and spatial distribution using an independent test set, with the effectiveness validated through typical cloud system case studies and statistical analysis.

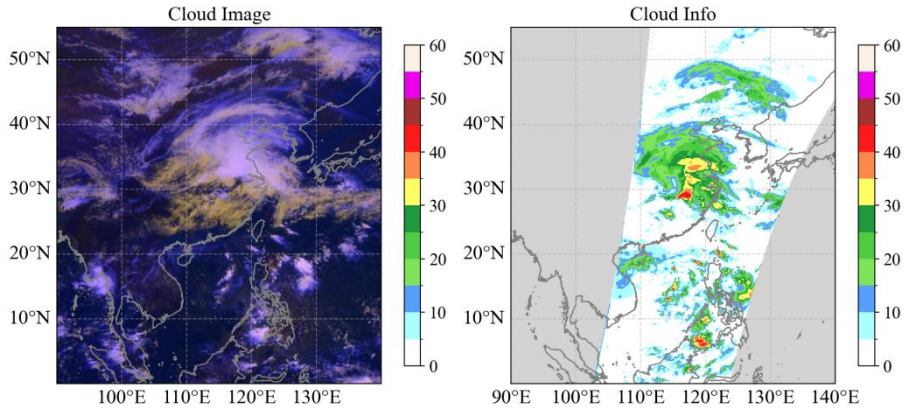

(**a**) (**b**)

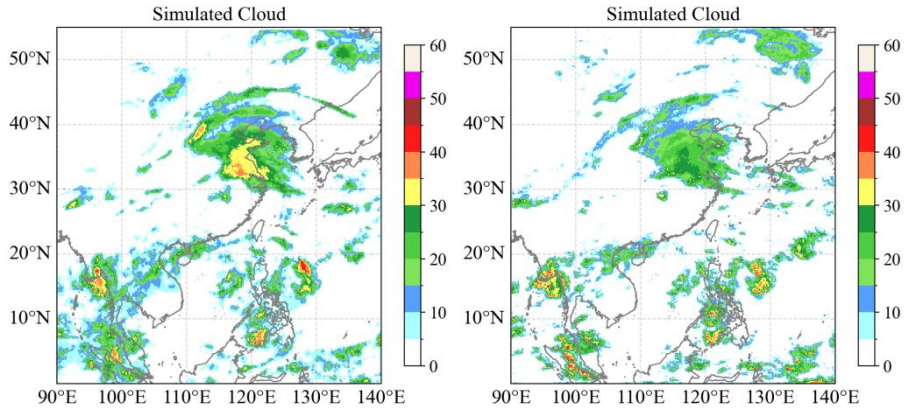

(c) (d)

Figure 3 Remote sensing data and optical thickness retrieval results, taking the results at 2:30 on May 8, 2025, as an example. (a) FY-4B visible light image; (b) FY-3F cloud optical thickness product; (c) Cloud optical thickness retrieval results of Model A; (d) Cloud optical thickness retrieval results of Model B.

As illustrated in Figure 3, Figure a is the visible light image from the FY-4B geostationary satellite, and Figure b is the cloud optical thickness image retrieved from the FY-3F polar-orbiting satellite. Figures c and d show the outputs of Model A and Model B, respectively. It can be observed from the figure that the application of the neural network models extends the detection coverage of the polar-orbiting satellite. Given that the FY-3F polar-orbiting satellite passes over the same region only once per day, resulting in sparse observational data, the use of neural network models significantly addresses this limitation and effectively captures the spatial distribution characteristics of cloud systems.

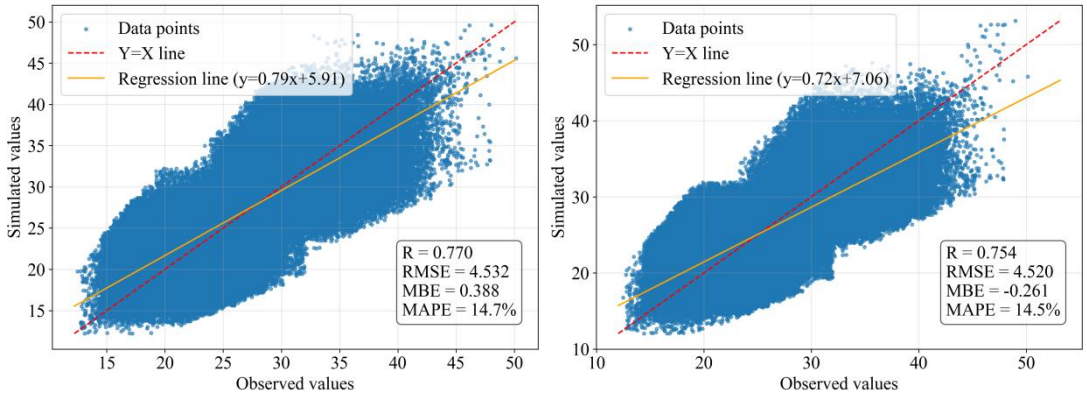

(a) (b)

Figure 4 Regression scatter plots for the test set of the two models. (a) Results of Model A; (b) Results of Model B.

As shown in Figure 4, the relationship between the cloud optical thickness retrieved by the models and the actual observations is presented in the form of scatter plots. The horizontal axis represents the observed values (ground truth), while the vertical axis represents the simulated values (model retrievals). Ideally, all points should lie near the y = x diagonal line; the closer and more concentrated the points are

around this diagonal, the higher the model accuracy. The scatter points of Model A are tightly distributed around the y = x diagonal across a wide range, indicating high accuracy and low systematic error in cloud optical thickness retrieval. In contrast, the scatter points of Model B are predominantly located below the diagonal, with the retrieved values generally lower than the observations, revealing a clear systematic underestimation, along with a narrower dynamic range of the retrieved values. These results demonstrate that both models are capable of achieving spatiotemporal extension of polar-orbiting satellite cloud optical thickness, yet Model A exhibits superior quantitative accuracy.

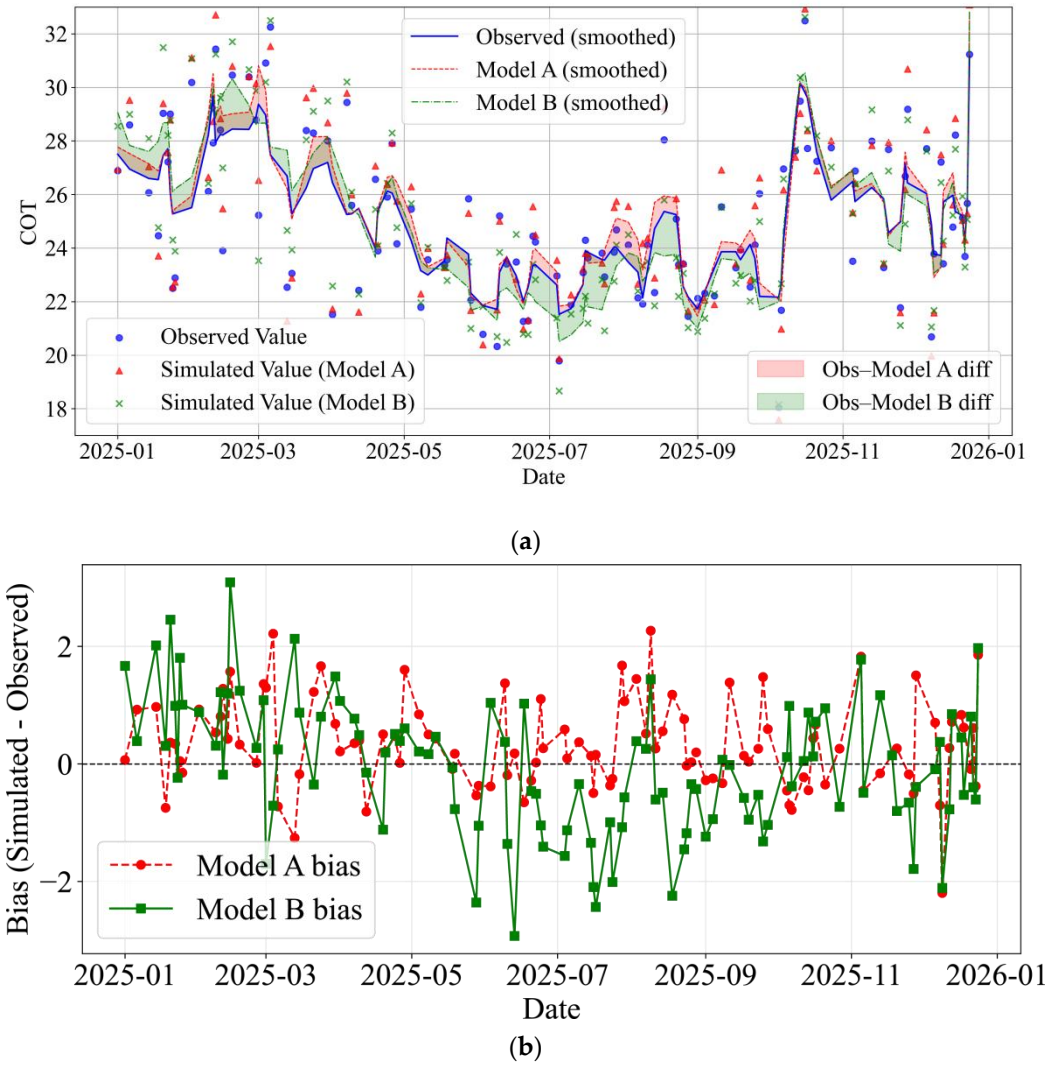

Figure 5 Daily mean distribution of the two models on the test set. (a) Distribution results of the two models; (b) Difference between the two models and the observations.

In the initial model design, training and test sets were established for each month. Figure 5a presents the daily mean distribution of the two models (Model A and Model B) on the test set, along with their differences from the observations, to evaluate the temporal consistency and bias characteristics of the model retrieval results. The horizontal axis represents the date (from January 2025 to January 2026), and the vertical axis represents the daily mean cloud optical thickness (COT), with the curves

showing the 7-point smoothed results of the scatter points. In terms of distribution trends, the simulated values of Model A (red triangles) exhibit a high degree of consistency with the observations (blue circles) in daily variation, covering a wide range with closely matched values. Although the simulated values of Model B (green crosses) show a generally similar trend, the deviation is slightly larger. Figure 5b shows the differences between the two models and the observations. Model A demonstrates a high alignment with the observations in daily variation, with smaller and more stable errors (narrow and uniform difference range), whereas Model B exhibits systematic underestimation (with simulated values generally lower than the observations).

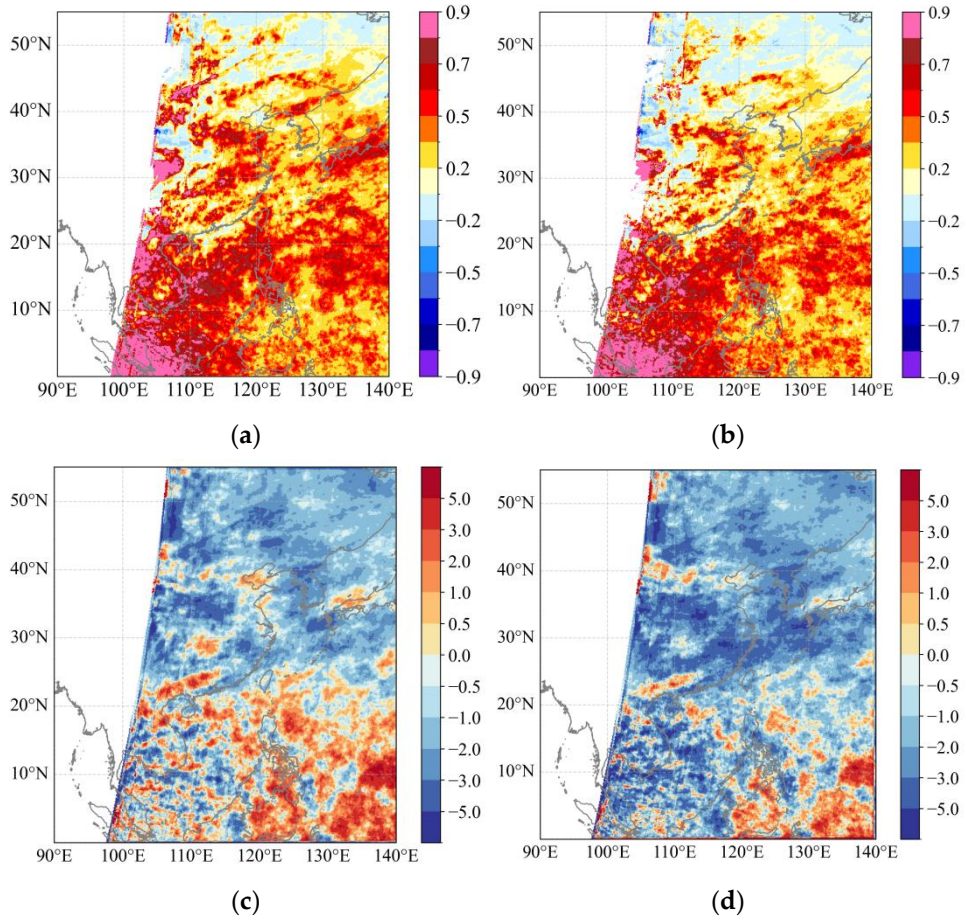

Figure 6 Statistical results of the two models against the measured data. (a) Temporal correlation coefficient between Model A and the measured data; (b) Temporal correlation coefficient between Model B and the measured data; (c) Mean error distribution between Model A and the measured data; (d) Mean error distribution between Model B and the measured data.

Figure 6 presents the statistical results between the two models (Model A and Model B) and the measured data on the test set. Figures a and b show the correlation coefficient distributions of Model A and Model B with respect to the measured data, respectively, while Figures c and d show the mean error distributions of the differences between Model A and Model B and the measured data, respectively. Figures a and b indicate that both Model A and Model B exhibit an overall positive correlation with the measured data, with some negative correlations observed in

regions north of 30°N. The spatial correlation coefficient of Model A is slightly higher than that of Model B. Figures c and d show that for Model B, the differences from the measured data are predominantly negative across most regions. For Model A, the differences from the measured data are negative in regions north of 30°N and positive in regions south of 30°N.

5.Discussion

5.1 Model Performance Advantages and Limitations

In this study, two neural network models based on FY-4B multi-channel data are proposed to achieve end-to-end retrieval of cloud optical thickness. The key advantage lies in overcoming the spatiotemporal resolution limitations of the polar-orbiting satellite FY-3F. By leveraging the minute-scale, wide-coverage observation characteristics of geostationary satellites, the proposed approach accomplishes spatiotemporal extension retrieval of cloud optical thickness, addressing the challenges of traditional physical methods such as reliance on prior parameters, slow operational response, and limited scenario adaptability. This provides an efficient machine learning solution for real-time retrieval of cloud optical thickness.

Although both models achieve effective retrieval, notable limitations remain. Model A demonstrates superior overall quantitative accuracy but exhibits a weak negative correlation in high-latitude regions, which may be attributed to the training data being concentrated in the time window of UTC 2:00–2:30, where such regions are predominantly under nighttime conditions. Additionally, its retrieval accuracy for extremely thick convective clouds (COT > 40) still requires improvement, as the dispersion of simulated results in high-value areas remains to be reduced. Model A, in contrast, exhibits pronounced systematic underestimation, which is speculated to result from overfitting to three-dimensional spatiotemporal features due to its full-extraction architecture, leading to insufficient signal response for high-value cloud systems. Furthermore, its spatial consistency is inferior to that of Model A, with retrieval errors being more pronounced in regions characterized by strong cloud inhomogeneity.

5.2 Targeted Optimization Strategies

To address the aforementioned limitations, lightweight optimization strategies are proposed from three aspects: model architecture, dataset, and training strategy.

Model architecture: A multi-scale feature fusion module (e.g., multi-kernel Conv3D) is introduced into Model A to enhance its feature representation capability for complex cloud systems in high-latitude regions. For Model B, an SE attention mechanism is embedded to guide the model in focusing on key features relevant to cloud optical thickness retrieval while suppressing redundant information, thereby

alleviating the systematic underestimation issue.

Dataset: Samples from high-latitude and complex terrain regions are supplemented to improve the model's adaptability to varying illumination and topographic conditions. Multi-source data, including FY-3F cloud phase products and ground-based observations, are integrated to impose additional physical constraints on extreme cloud system retrieval.

Training strategy: Adversarial training is employed to reduce model overfitting to specific cloud types. A spatial smoothing term is incorporated into the loss function to enhance the spatial consistency of retrieval results.

5.3 Future Work

In future work, the models will be refined based on the proposed optimization strategies and validated globally to further improve their generalization capability. Collaborative retrieval methods leveraging multi-source data from FY-4B, FY-3F, and other Fengyun series satellites will be explored to achieve accurate cloud optical thickness retrieval with high spatiotemporal resolution. Additionally, the retrieval results will be integrated with numerical weather prediction models to investigate their practical applicability in nowcasting of short-term heavy precipitation and identification of severe convective cloud clusters, thereby providing higher-quality cloud parameters for operational meteorological applications.

In summary, this study demonstrates the feasibility and advantages of machine learning methods for satellite-based cloud optical thickness retrieval. The identified model limitations and the proposed optimization strategies offer valuable insights for future research on intelligent retrieval of cloud remote sensing parameters.

6 Conclusions

This study proposes a machine learning-based method for retrieving cloud optical thickness (COT) using multi-channel data from the FY-4B geostationary satellite. High-precision COT products from the polar-orbiting FY-3F satellite are employed as ground truth labels to construct a spatiotemporally matched training dataset. Two models are designed: Model A, which adopts a decoupled feature extraction strategy, and Model B, which performs full three-dimensional feature extraction, enabling end-to-end COT retrieval. This approach effectively addresses the limitations of traditional physical retrieval methods, such as dependence on prior parameters, slow operational response, and limited scenario adaptability, while also overcoming the spatiotemporal resolution constraints of polar-orbiting satellites. Leveraging the minute-scale, wide-coverage observational advantages of FY-4B, this method achieves spatiotemporal extension retrieval of COT.

Experimental results demonstrate that both models effectively retrieve COT, with Model A exhibiting superior performance. For Model A, the correlation coefficient

with observed values reaches 0.770, with an RMSE of 4.532. Its temporal variation trends are highly consistent with observations, and it demonstrates better spatial correlation and more stable errors. Although Model B captures the overall distribution characteristics of COT, it suffers from systematic underestimation, with a correlation coefficient of 0.754 and slightly inferior spatial consistency compared to Model A. The decoupled feature extraction strategy, which prioritizes the vertical dimension, more efficiently captures the core features of COT while reducing computational redundancy, making it better suited for COT retrieval compared to the full three-dimensional feature extraction architecture.

This study validates the feasibility and practicality of machine learning methods for satellite-based COT retrieval, offering a novel approach for the intelligent retrieval of cloud parameters from geostationary satellites. Future efforts involving model architecture optimization, dataset expansion, and training strategy improvements can further enhance retrieval accuracy and spatial consistency for complex high-latitude scenarios and extreme cloud systems. Applying the optimized models to multi-satellite collaborative retrieval and integrating them with numerical weather prediction models can achieve accurate COT retrieval with high spatiotemporal resolution, providing high-quality cloud parameter support for meteorological operations and research, including nowcasting of short-term heavy precipitation, identification of severe convective cloud clusters, and atmospheric radiation budget calculations.

Data Availability Statement: The FY satellite data used in this study are available from the Fengyun Satellite Data Center (http://fy4.nsmc.org.cn/).

Conflicts of Interest: The authors declare no conflicts of interest.

References

[1] Kox, S., Bugliaro, L., & Ostler, A. (2014). Retrieval of cirrus cloud optical thickness and top altitude from geostationary remote sensing. Atmospheric Measurement Techniques, 7(10), 3233-3246.

[2] Hong, G., Yang, P., Huang, H. L., Baum, B. A., Hu, Y., & Platnick, S. (2007). The sensitivity of ice cloud optical and microphysical passive satellite retrievals to cloud geometrical thickness. IEEE Transactions on Geoscience and Remote Sensing, 45(5), 1315-1323.

[3] Iwabuchi, H., & Hayasaka, T. (2002). Effects of cloud horizontal inhomogeneity on the optical thickness retrieved from moderate-resolution satellite data. Journal of the Atmospheric Sciences, 59(14), 2227-2242.

[4] Wei, H., Yang, P., Li, J., Baum, B. A., Huang, H. L., Platnick, S., Hu, Y., & Strow, L. (2004). Retrieval of semitransparent ice cloud optical thickness from Atmospheric Infrared Sounder (AIRS) measurements. IEEE Transactions on Geoscience and Remote Sensing, 42(10), 2254-2267.

[5] Platnick, S., & Valero, F. P. (1995). A validation of a satellite cloud retrieval during ASTEX. Journal of Atmospheric Sciences, 52(16), 2985-3001.

[6] Wei, X.; Liu, Y.; Cheng, C.; Chang, X.; Guo, J. Topographic Precipitation Diagnosis: Model Design and Validation in a Two-Dimensional Context. Atmosphere 2025, 16, 593. https://doi.org/10.3390/atmos16050593
[7] Wang, C., Yang, P., Baum, B. A., Platnick, S., Heidinger, A. K., Hu, Y., & Holz, R. E. (2011). Retrieval of ice cloud optical thickness and effective particle size using a fast infrared radiative transfer model. Journal of Applied Meteorology and Climatology, 50(11), 2283-2297.
[8] Vukicevic, T., Coddington, O., & Pilewskie, P. (2010). Characterizing the retrieval of cloud properties from optical remote sensing. Journal of Geophysical Research: Atmospheres, 115(D20), D20203.
[9] Wei, X.; Liu, Y.; Chang, X.; Guo, J.; Li, H. Mechanism Study of Two-Dimensional Precipitation Diagnostic Models Within a Dynamic Framework. Atmosphere 2025, 16, 380. https://doi.org/10.3390/atmos16040380
[10] Coddington, O. M., Pilewskie, P., Redemann, J., Platnick, S., Russell, P. B., Schmidt, K. S., Gore, W. J., Livingston, J., Wind, G., & Vukicevic, T. (2010). Examining the impact of overlying aerosols on the retrieval of cloud optical properties from passive remote sensing. Journal of Geophysical Research: Atmospheres, 115(D10), D10211.
[11] Wei Xiangqian, Yi Liu, Jun Guo, Xinyu Chang, and Haochuan Li. Applicability Study of Euler–Lagrange Integration Scheme in Constructing Small-Scale Atmospheric Dynamics Models. Atmosphere 2024, 15, 644. https://doi.org/10.3390/atmos15060644
[12] Wei, X., Chang, N. B., Bai, K., & Gao, W. (2020). Satellite remote sensing of aerosol optical depth: Advances, challenges, and perspectives. Critical Reviews in Environmental Science and Technology, 50(16), 1640-1725.
[13] Poulsen, C. A., Siddans, R., Thomas, G. E., Sayer, A. M., Grainger, R. G., Campmany, E., Dean, S. M., Arnold, C., & Watts, P. D. (2012). Cloud retrievals from satellite data using optimal estimation: Evaluation and application to ATSR. Atmospheric Measurement Techniques, 5(8), 1889-1910.
[14] Jethva, H., Torres, O., Remer, L. A., & Bhartia, P. K. (2013). A color ratio method for simultaneous retrieval of aerosol and cloud optical thickness of above-cloud absorbing aerosols from passive sensors: Application to MODIS measurements. IEEE Transactions on Geoscience and Remote Sensing, 51(7), 3862-3870.
[15] Krisna, T. C., Wendisch, M., Ehrlich, A., Jäkel, E., Werner, F., Weigel, R., Borrmann, S., Mahnke, C., Pöschl, U., Andreae, M. O., & Voigt, C. (2018). Comparing airborne and satellite retrievals of cloud optical thickness and particle effective radius using a spectral radiance ratio technique: Two case studies for cirrus and deep convective clouds. Atmospheric Chemistry and Physics, 18(7), 4439-4462.
[16] Wang, W., Shi, C., Shang, H., Yin, S., Xu, J., Xu, N., Chen, L., & Letu, H. (2024). Development of an algorithm for the simultaneous retrieval of cloud-top height and cloud optical thickness combining radiative transfer and multisource satellite information from O_4 hyperspectral measurements. IEEE Transactions on Geoscience and Remote Sensing, 62, 1-11.
[17] Rozanov, V. V., & Kokhanovsky, A. A. (2004). Semianalytical cloud retrieval algorithm as applied to the cloud top altitude and the cloud geometrical thickness determination from top-of-atmosphere reflectance measurements in the oxygen A band. Journal of Geophysical Research: Atmospheres, 109(D5), D05202.
[18] Iwabuchi, H., & Hayasaka, T. (2003). A multi-spectral non-local method for retrieval of boundary layer cloud properties from optical remote sensing data. Remote

Sensing of Environment, 88(3), 294-308.
[19] Xiangqian Wei. Retrieving 3D Humidity Profiles from FY-2F Geostationary Satellite Infrared Images Using a Deep Learning Fusion Model[Preprint]. ChinaXiv, 2026. DOI: 10.12074/202604.00287.
[20] Zheng, J., Wang, G., He, W., Yu, Q., Liu, Z., Lin, H., Li, S., & Wen, B. (2026). Daytime sea fog detection in the South China Sea based on machine learning and physical mechanism using Fengyun-4B meteorological satellite. Remote Sensing, 18(2), 336.
[21] Yang, H., & Guan, L. (2025). Optimal channel selection for FY-4B GIIRS explainable machine learning cloud detection algorithm. IEEE Transactions on Geoscience and Remote Sensing.
[22] Qu, J., Ye, L., Yan, J., Sun, J., & Huyan, Z. (2025). Research on cloud detection method based on voting ensemble learning using FY-4B satellite data. Geocarto International, 40(1), 2487012.
[23] Xia, J., & Guan, L. (2024). Retrieval of cloud fraction using machine learning algorithms based on FY-4A AGRI observations. Atmospheric Measurement Techniques, 17(22), 6697-6706.
[24] Huang, Y., Bao, Y., Petropoulos, G. P., Lu, Q., Huo, Y., & Wang, F. (2024). Precipitation estimation using FY-4B/AGRI satellite data based on random forest. Remote Sensing, 16(7), 1267.
[25] Liu, N., Jiang, J., Mao, D., Fang, M., Li, Y., Han, B., & Ren, S. (2024). Artificial intelligence-based precipitation estimation method using fengyun-4b satellite data. Remote Sensing, 16(21), 4076.
[26] Xia, D., Zhao, D., Li, K., Qiu, Z., Liu, J., Luan, J., Chen, S., Song, B., Wang, Y., & Yang, J. (2025). Retrieval of cloud optical thickness during nighttime from FY-4B AGRI using a convolutional neural network. Remote Sensing, 17(5), 737.
[27] Li, Y., Han, W., Duan, W., Li, Z., & Li, H. (2025). A machine learning–based observation operator for FY−4B GIIRS brightness temperatures considering the uncertainty of label data. Journal of Geophysical Research: Machine Learning and Computation, 2(1), e2024JH000449.
[28] Yang, J., Qiu, Z., Zhao, D., Xu, N., Wang, Y., & Li, K. (2026). CACM-Net++: FY-4B AGRI day and night cloud mask algorithm modeling. IEEE Transactions on Geoscience and Remote Sensing.